

Role of near-field enhancement in plasmonic laser nanoablation using gold nanorods on a silicon substrate

R. K. Harrison and Adela Ben-Yakar*

Department of Mechanical Engineering, University of Texas at Austin, 1 University Station C2200, Austin, 78712, Texas, USA

*ben-yakar@mail.utexas.edu

Abstract: We present experimental results for the plasmonic laser ablation of silicon with nanoscale features as small as 22 x 66 nm using single near-infrared, femtosecond laser pulses incident on gold nanorods. Near the ablation threshold, these features are photo-imprints of gold nanorod particles positioned on the surface of the silicon and have feature sizes similar to the nanorods. The single rod-shaped ablation pattern matches the enhancement patterns of the Poynting vector magnitude on the surface of silicon, implying that the ablation is a result of the plasmonic enhancement of the incident electromagnetic waves in the near-field of the particles. Interestingly, the ablation pattern is different from the two separated holes at the ends of the nanorod, as would be expected from the electric field – $|E|^2$ enhancement pattern. We measured the plasmonic ablation threshold fluence to be almost two orders of magnitude less than the femtosecond laser ablation threshold of silica, present in the thin native oxide layer on the surface of silicon. This value also agrees with the enhancement of the Poynting vector of a nanorod on silicon as calculated with electromagnetic simulations. We thus conclude that plasmonic ablation with plasmonic nanoparticles depends directly on the polarization and the value of the near-field enhancement of the Poynting vector and not the square of the electric field as previously suggested.

©2010 Optical Society of America

OCIS codes: (350.3390) Laser materials processing; (220.4241) Nanostructure formation; (320.2250) Femtosecond phenomena; (190.7110) Ultrafast nonlinear optics; (310.6628) Subwavelength structures, nanostructures; (250.5403) Plasmonics; (160.4236) Nanomaterials.

References and links

1. C. Tan, C. S. Peng, J. Pakarinen, M. Pessa, V. N. Petryakov, Y. K. Verevkin, J. Zhang, Z. Wang, S. M. Olaizola, T. Berthou, and S. Tisserand, "Ordered nanostructures written directly by laser interference," *Nanotechnology* **20**(12), 125303 (2009).
2. A. Chimmalgi, T. Y. Choi, C. P. Grigoropoulos, and K. Komvopoulos, "Femtosecond laser aperturless near-field nanomachining of metals assisted by scanning probe microscopy," *Appl. Phys. Lett.* **82**(8), 1146 (2003).
3. J. Serbin, A. Egbert, A. Ostendorf, B. N. Chichkov, R. Houbertz, G. Domann, J. Schulz, C. Cronauer, L. Fröhlich, and M. Popall, "Femtosecond laser-induced two-photon polymerization of inorganic-organic hybrid materials for applications in photonics," *Opt. Lett.* **28**(5), 301–303 (2003).
4. A. P. Joglekar, H. H. Liu, E. Meyhöfer, G. Mourou, and A. J. Hunt, "Optics at critical intensity: applications to nanomorphing," *Proc. Natl. Acad. Sci. U.S.A.* **101**(16), 5856–5861 (2004).
5. H. J. Münzer, M. Mosbacher, M. Bertsch, O. Dubbers, F. Burmeister, A. Pack, R. Wannemacher, and B. U. Runge, D. Bäuerle, J. Boneberg, and P. Leiderer, "Optical near field effects in surface nanostructuring and laser cleaning," *Proc. SPIE* **4426**, 180–183 (2002).
6. D. Brodoceanu, L. Landström, and D. Bäuerle, "Laser-induced nanopatterning of silicon with colloidal monolayers," *Appl. Phys., A Mater. Sci. Process.* **86**(3), 313–314 (2007).
7. N. N. Nedyalkov, P. A. Atanasov, and M. Obara, "Near-field properties of a gold nanoparticle array on different substrates excited by a femtosecond laser," *Nanotechnology* **18**(30), 305703 (2007).
8. D. Eversole, B. Luk'yanchuk, and A. Ben-Yakar, "Plasmonic laser nanoablation of silicon by the scattering of femtosecond pulses near gold nanospheres," *Appl. Phys. A: Mater. Sci. Process.* **89**(2), 283–291 (2007).

9. H. Wang, Y. Wu, B. Lassiter, C. L. Nehl, J. H. Hafner, P. Nordlander, and N. J. Halas, "Symmetry breaking in individual plasmonic nanoparticles," *Proc. Natl. Acad. Sci. U.S.A.* **103**(29), 10856–10860 (2006).
10. C. Sönnichsen, T. Franzl, T. Wilk, G. von Plessen, J. Feldmann, O. Wilson, and P. Mulvaney, "Drastic reduction of plasmon damping in gold nanorods," *Phys. Rev. Lett.* **88**(7), 077402 (2002).
11. T. R. Jensen, M. D. Malinsky, C. L. Haynes, and R. P. Van Duyne, "Nanosphere Lithography: Tunable Localized Surface Plasmon Resonance Spectra of Silver Nanoparticles," *J. Phys. Chem. B* **104**(45), 10549–10556 (2000).
12. K. L. Kelly, E. Coronado, L. L. Zhao, and G. C. Schatz, "The Optical Properties of Metal Nanoparticles: The Influence of Size, Shape, and Dielectric Environment," *J. Phys. Chem. B* **107**(3), 668–677 (2003).
13. N. J. Durr, T. Larson, D. K. Smith, B. A. Korgel, K. Sokolov, and A. Ben-Yakar, "Two-photon luminescence imaging of cancer cells using molecularly targeted gold nanorods," *Nano Lett.* **7**(4), 941–945 (2007).
14. A. L. Oldenburg, M. N. Hansen, D. A. Zweifel, A. Wei, and S. A. Boppart, "Plasmon-resonant gold nanorods as low backscattering albedo contrast agents for optical coherence tomography," *Opt. Express* **14**(15), 6724–6738 (2006).
15. P. Zijlstra, J. W. M. Chon, and M. Gu, "Five-dimensional optical recording mediated by surface plasmons in gold nanorods," *Nature* **459**(7245), 410–413 (2009).
16. N. Arnold, "Influence of the substrate, metal overlayer and lattice neighbors on the focusing properties of colloidal microspheres," *Appl. Phys. A: Mater. Sci. Process.* **92**(4), 1005–1012 (2008).
17. T. Sakai, T. Miyanishi, N. Nedyalkov, Y. Nishizawa, and M. Obara, "Nano-dimple processing of silicon surfaces by femtosecond laser irradiation with dielectric particle templates in the Mie scattering domain," *J. Phys. D* **42**(2), 025502 (2009).
18. B. S. Luk'yanchuk, N. Arnold, S. M. Huang, Z. B. Wang, and M. H. Hong, "Three-dimensional effects in dry laser cleaning," *Appl. Phys., A Mater. Sci. Process.* **77**, 209–215 (2003).
19. A. Plech, V. Kotaidis, M. Lorenc, and J. Boneberg, "Femtosecond laser near-field ablation from gold nanoparticles," *Nat. Phys.* **2**(1), 44–47 (2006).
20. A. Ben-Yakar, and R. L. Byer, "Femtosecond laser ablation properties of borosilicate glass," *J. Appl. Phys.* **96**(9), 5316–5323 (2004).
21. H. Urey, "Spot size, depth-of-focus, and diffraction ring intensity formulas for truncated Gaussian beams," *Appl. Opt.* **43**(3), 620–625 (2004).
22. P. P. Pronko, P. A. VanRompay, C. Horvath, F. Loesel, T. Juhasz, X. Liu, and G. Mourou, "Avalanche ionization and dielectric breakdown in silicon with ultrafast laser pulses," *Phys. Rev. B* **58**(5), 2387–2390 (1998).
23. S. Besner, "Surface modifications during femtosecond laser ablation in vacuum, air, and water," *Proc. SPIE* **5578**, 554–558 (2004).
24. D. Giguère, G. Olivié, F. Vidal, S. Toetsch, G. Girard, T. Ozaki, J. C. Kieffer, O. Nada, and I. Brunette, "Laser ablation threshold dependence on pulse duration for fused silica and corneal tissues: experiments and modeling," *J. Opt. Soc. Am. A* **24**(6), 1562–1568 (2007).
25. I. Chowdhury, A. Wu, X. Xu, and A. Weiner, "Ultra-fast laser absorption and ablation dynamics in wide-band-gap dielectrics," *Appl. Phys. A: Mater. Sci. Process.* **81**(8), 1627–1632 (2005).
26. Y. Wang, X. Xu, and L. Zheng, "Molecular dynamics simulation of ultrafast laser ablation of fused silica film," *Appl. Phys., A Mater. Sci. Process.* **92**(4), 849–852 (2008).
27. S. E. Kirkwood, M. R. Shadnam, A. Amirfazli, and R. Fedosejevs, "Mechanism for femtosecond laser pulse patterning of self-assembled monolayers on gold-coated substrates," *J. Phys. Conf. Ser.* **59**, 428–431 (2007).
28. X. Ni, C. Wang, L. Yang, J. Li, L. Chai, W. Jia, R. Zhang, and Z. Zhang, "Parametric study on femtosecond laser pulse ablation of Au films," *Appl. Surf. Sci.* **253**(3), 1616–1619 (2006).
29. S. Amoruso, X. Wang, C. Altucci, C. De Lisio, M. Armenante, R. Bruzzese, N. Spinelli, and R. Velotta, "Double-peak distribution of electron and ion emission profile during femtosecond laser ablation of metals," *Appl. Surf. Sci.* **186**(1-4), 358–363 (2002).
30. S. Wellershoff, J. Hohlfeld, J. Gädde, and E. Matthias, "The role of electron–phonon coupling in femtosecond laser damage of metals," *Appl. Phys. A: Mater. Sci. Process.* **69**, S99–S107 (1999).
31. B. T. Draine, "The discrete-dipole approximation and its application to interstellar graphite grains," *Astrophys. J.* **333**, 848–872 (1988).
32. A. Penttilä, E. Zubko, K. Lumme, K. Muinonen, M. A. Yurkin, B. Draine, J. Rahola, A. G. Hoekstra, and Y. Shkuratov, "Comparison between discrete dipole implementations and exact techniques," *JQSRT* **106**, 417–436 (2007).
33. B. T. Draine, and J. C. Weingartner, "Radiative torques on interstellar grains. I. Superthermal spin-up," *Astrophys. J.* **470**, 551–565 (1996).
34. P. K. Jain, K. S. Lee, I. H. El-Sayed, and M. A. El-Sayed, "Calculated absorption and scattering properties of gold nanoparticles of different size, shape, and composition: applications in biological imaging and biomedicine," *J. Phys. Chem. B* **110**(14), 7238–7248 (2006).
35. M. A. Yurkin, V. P. Maltsev, and A. G. Hoekstra, "The discrete dipole approximation for simulation of light scattering by particles much larger than the wavelength," *JQSRT* **106**, 546–557 (2007).
36. E. D. Palik, ed., *Handbook of Optical Constants of Solids* (Academic, New York, 1985).
37. L. B. Scaffardi, and J. O. Tocho, "Size dependence of refractive index of gold nanoparticles," *Nanotechnology* **17**(5), 1309–1315 (2006).
38. E. A. Coronado, and G. C. Schatz, "Surface plasmon broadening for arbitrary shape nanoparticles: A geometrical probability approach," *J. Chem. Phys.* **119**(7), 3926–3934 (2003).

39. M. A. Yurkin, D. de Kanter, and A. G. Hoekstra, "Accuracy of the discrete dipole approximation for simulation of optical properties of gold nanoparticles," *J. Nanophotonics* **4**(1), 041585 (2010).
40. J. D. Jackson, *Classical Electrodynamics* (Wiley, New York, 1975).
41. C. F. Bohren, and D. Huffman, *Absorption and Scattering of Light by Small Particles* (Wiley, New York, 1983).
42. M. A. Yurkin, and A. G. Hoekstra, "The discrete dipole approximation: an overview and recent developments," *JQSRT* **106**, 558–589 (2007).
43. B. T. Draine, and P. J. Flatau, "Discrete-dipole approximation for scattering calculations," *J. Opt. Soc. Am. A* **11**(4), 1491–1499 (1994).
44. J. H. Kim, S. H. Ehrman, G. W. Mulholland, and T. A. Germer, "Polarized light scattering by dielectric and metallic spheres on silicon wafers," *Appl. Opt.* **41**(25), 5405–5412 (2002).
45. P. A. Bobbert, and J. Vlieger, "Light scattering by a sphere on a substrate," *Physica A* **137**(1-2), 209–242 (1986).
46. C. Ungureanu, R. G. Rayavarapu, S. Manohar, and T. G. van Leeuwen, "Discrete dipole approximation simulations of gold nanorod optical properties: Choice of input parameters and comparison with experiment," *J. Appl. Phys.* **105**(10), 102032 (2009).
47. S. W. Prescott, and P. Mulvaney, "Gold nanorod extinction spectra," *J. Appl. Phys.* **99**(12), 123504 (2006).
48. E. Cappelli, S. Orlando, D. Sciti, M. Montozzi, and L. Pandolfi, "Ceramic surface modifications induced by pulsed laser treatment," *Appl. Surf. Sci.* **154-155** (1-4), 682–688 (2000).
49. K. Sokolowski-Tinten, J. Bialkowski, A. Cavalleri, D. von der Linde, A. Oparin, J. Meyer-ter-Vehn, and S. I. Anisimov, "Transient states of matter during short pulse laser ablation," *Phys. Rev. Lett.* **81**(1), 224–227 (1998).
50. S. Link, C. Burda, B. Nikoobakht, and M. A. El-Sayed, "How long does it take to melt a gold nanorod? A femtosecond pump-probe absorption spectroscopic study," *Chem. Phys. Lett.* **315**(1-2), 12–18 (1999).
51. A. Ben-Yakar, A. Harkin, J. Ashmore, R. L. Byer, and H. A. Stone, "Thermal and fluid processes of a thin melt zone during femtosecond laser ablation of glass: the formation of rims by single laser pulses," *J. Phys. D* **40**(5), 1447–1459 (2007).

1. Introduction

As conventional lithography reaches its limits, there is an urgent need for alternative approaches to create features on the nanometer scale. New laser-based techniques have proven their ability to work on the nanometer scale beyond the diffraction limit using interference and nonlinear optical techniques such as interference lithography, scanning near-field optical microscopy, and two-photon polymerization [1–3].

Ablation with ultrafast lasers with pulse durations below 10 ps offers strong advantages for nanofabrication. Focused ultrafast laser pulses can have high enough intensities to generate 'seed' free electrons through multiphoton ionization, resulting in the ability to ablate any material, including high-bandgap transparent dielectrics. Since the pulse length for ultrafast lasers is much shorter than the electron-phonon thermalization time scale, the ablation process is more efficient and requires very small pulse energies to initiate ablation. These unique features of ultrafast laser ablation provide the ability to fabricate more precise features on surfaces with a reduced heat-affected zone surrounding the ablated region. Researchers have created features as small as 40 nm with direct ultrafast laser ablation by using Gaussian beams and intensities just slightly over the ablation threshold [4]. However, direct laser ablation is limited by the pulse-to-pulse laser stability and the limitation of having just a single tightly focused beam that creates patterns serially. To overcome this limitation, many groups have used near-field patterning using a self-assembled monolayer of nanospheres. Dielectric spheres are assembled on a surface and subjected to large-beam ultrafast laser exposure to create arrays of localized ablation sites, as demonstrated in some recent interesting studies [5,6]. In these studies, the dielectric spheres act as focusing elements, leading to surface ablation underneath the spheres. This process becomes less efficient as the dielectric spheres decrease in size, and limited enhancement in the focal region reduces the usefulness of this technique for the creation of ultrasmall features. Several recent studies by our group and others have shown the use of plasmonic enhancement of spherical gold nanoparticles with ultrafast lasers to create sub-diffraction limited features on glass and silicon surfaces [7,8]. In this method, the plasmonic focusing properties of nanoparticles provide localized, highly enhanced near-field intensities strong enough to lead to nanoscale ablation for femtosecond (fs) pulses. The near-field enhancement region and corresponding possible feature size scale with the size of the nanoparticle, and there are no fundamental physical limits to prevent even smaller features from being created with this technique. Plasmonic nanoparticles are of great interest because of their strong interaction with light, resulting in uses ranging from biological contrast agents to solar concentrators.

Recent studies have focused significant effort towards understanding the plasmonic properties of non-spherical ‘broken symmetry’ nanoparticles [9–12]. Asymmetrical nanostructures are interesting mainly because they can provide large near-field enhancements and access to polarization and orientation effects not available in spherical particles. Gold nanorods have been used extensively in recent years for photonic and biomedical studies [13–15]. Unlike spheres, nanorods exhibit two resonances: a transverse and larger longitudinal resonance at longer wavelengths, depending strongly on both the diameter and the aspect ratio. By changing the geometry of the rods, the central wavelength of their longitudinal resonances can be tuned from visible to near-infrared wavelengths. Both photonics and biomedical communities have proposed to use these interesting tunability properties of gold nanorods in recent years for applications ranging from two-photon luminescence imaging to optical data storage [13,15]. Few studies, however, have examined the strong electromagnetic near-field enhancement also present for plasmonic nanoparticles.

The direct cause for plasmon-assisted near-field ablation is poorly understood, though the phenomenon has been demonstrated by several groups. Ablation can occur in the near-field of plasmonic nanoparticles when coupled with high-intensity ultrafast laser pulses. In this case, localized, sub-diffraction limited features can be created on a surface due to enhanced near-fields around a plasmonic nanoparticle. The near-field enhancement is the ratio of the near-field strength to the incident laser intensity. Since there is a constant relationship between the electric and magnetic fields for a plane wave of light, the intensity is often given as proportional to the square of the electric field – $|E|^2$. Another metric of the field strength is the Poynting vector, which is the cross-product of the electric and magnetic fields and has the magnitude of the local electromagnetic energy density ($|P|$). Both the electric field ($|E|^2$) enhancement and the Poynting vector magnitude have been identified as the dominant term for ablation. Several studies have evaluated the Poynting vector and electric field enhancement for near-field ablation in the case of colloidal monolayers of dielectric spheres on a substrate [16,17].

For example, Luk’yanchuk *et al.* hypothesized that the Poynting vector travelling into the surface, representing energy density or flow, could be the dominant term for surface ablation for dielectric spheres on a surface subjected to ultrafast laser pulses [18]. On the other hand, Plech *et al.* showed ablation near the poles of gold spheres with fs laser pulses using *in situ* SAXS measurements and the authors proposed the E-field enhancement as the reason for ablation [19]. Other groups have also used the $|E|^2$ enhancement as a predictor of ablation [7]. In a previous work, we investigated plasmonic laser nanoablation (PLN) using gold nanospheres on a silicon surface and found that the reduction in threshold followed the Poynting vector magnitude on the surface [8]. However, the maxima in the Poynting vector and E-field enhancement occur in the same location for all of these studies using spheres, and therefore the effects of the Poynting vector and E-field cannot be distinguished from each other as a predictor of ablation, except in the magnitude. While all of these studies provided useful information on PLN, the use of nanorods can provide a more complete picture. By taking advantage of the ‘broken symmetry’ of gold nanorods, where the Poynting vector and E-field enhancement patterns are displaced from one another, we can determine the dominant term for ablation by looking at the morphology of the ablation pattern in addition to comparing the reduction in the ablation threshold with the near-field enhancement terms. Studying the plasmonic near-field enhancement of gold nanorods is also of special interest because of the strong resonance in the NIR, where fs-lasers are readily available (Ti:Sapphire) and which is in the ‘therapeutic window’ of biomedical interest.

In this study, we present the PLN of silicon with enhanced femtosecond laser pulses in the near-field of gold nanorods. The surface enhancement and corresponding ablation is strongly dependent on the beam polarization, nanorod orientation, and local environment near the nanoparticle. We measure nanoparticle near-field enhancements through a reduction in the threshold energy to create surface ablation and compare the results with our simulations.

2. Experimental methods

2.1 Optics

Single ultrafast laser pulses from a Ti:Sapphire laser ($\lambda = 780$ nm, $\tau = 184$ fs, *Spectra Physics, Spitfire*) irradiated gold nanorods on a silicon surface. The characterized beam quality revealed a Gaussian spatial beam profile with $M_x^2 = 1.09$ and $M_y^2 = 1.17$. We focused the laser beam on the sample using a low numerical aperture (NA) objective (NA = 0.28, 10X, Mitutoyo). To characterize the spot size on the sample, we measured the diameters of craters ablated with single laser pulses on silicon in the absence of nanoparticles as a function of laser fluence. Taking advantage of the logarithmic dependence of the square of the ablation crater diameter with the fluence for a Gaussian beam, we estimated the spot size on the sample in each experiment [20]. From this data, we measured a laser beam spot size radius at the focal plane of 2.57 ± 0.15 μm , compared with a theoretical minimum spot radius of 2.23 μm for a truncated Gaussian beam using our experimental conditions [21]. We then calculated the local fluence (peak fluence) present at each nanoparticle by using this spot size and a Gaussian beam profile.

2.2 Nanorod characterization

We used gold nanorods (Nanopartz) for our PLN experiments. The nanorods were nominally 25 nm in diameter with a longitudinal resonance peak at 756 nm. We characterized the nanorods using high-resolution SEM and scanning transmission electron microscopy (STEM) imaging (Hitachi S-5500). More than 200 individual particles were analyzed and the widths, lengths, shapes, and aspect ratios for each rod were compiled. The rods were slightly bone-shaped, had a maximum width near the ends, and had a minimum width at the waist. The average ratio of rod waist to maximum width was 0.87. From this data set, we found that the average length was 77 ± 4 nm, with an average width of 28 ± 2 nm, and a corresponding average aspect ratio of 2.8 ± 0.2 , using the averaged ratios of length and maximum nanorod diameters for each rod. The uncertainties given represent one standard deviation in the measured nanorods.

2.3 Materials

We diced silicon (100) wafers into 5×5 mm² sections with a diamond cutter and ultrasonically cleaned them using sulfuric acid and methanol. To identify individual ablation sites, we fabricated microscale grids on the silicon surface using a focused fs-laser beam and deposited a 10 μL aliquot of colloidal nanorods solution. Samples were imaged before and after fs-laser irradiation using high resolution field emission scanning electron microscopy (SEM) and atomic force microscopy (AFM) techniques. To minimize the effects of heating so that we could isolate the near-field effects for plasmonic ablation, we studied nanorods off-resonance in an air environment. In air, the resonance wavelength of nanorods is blue-shifted as compared with nanorods in an aqueous medium. The absorption of isolated rods is more than 20 times less in air than in water at 780 nm.

2.4 Fs laser ablation thresholds

Table 1 presents a summary of the fs-laser ablation thresholds for silicon (100), fused silica, and gold films of two different thicknesses obtained in our experiments and compared with data tabulated from other published studies. The thin gold films were fabricated through thermal evaporation onto a glass substrate, using a thin intermediary chrome layer to promote adhesion. We estimated the thresholds for single shot ablation according to the D^2 method [20]. In this method, the logarithmic dependence of the ablation diameter and fluence provided both the spot radius on the sample and threshold energy, thus a good estimate for the real threshold fluence. Using a minimum of 10 different pulse energies in all cases with the beam at normal incidence to the sample, we estimated the peak fluences at the ablation threshold. AFM analysis using the depth method for obtaining single shot ablation thresholds for silicon, presented in our previous work, yielded similar results [8]. In addition, these

values agree with other reported values, shown in Table 1. Our spot size and threshold uncertainties were determined from the linear regression analysis of all the spots measured for a sample.

All measurements use ultrafast lasers with wavelengths between 775 – 800 nm and pulse lengths from 90 – 300 fs [8,22–29]. We use peak fluences for the ablation thresholds, given as two times the energy divided by the spot area, in all cases throughout the paper.

Table 1. Single-shot ultrafast laser ablation thresholds of various materials.

<i>Material</i>	<i>Thickness</i>	<i>Ablation Threshold</i>	<i>Source</i>
Silicon (100)	Bulk	$0.42 \pm 0.06 \text{ J/cm}^2$	This work
Silicon (100)	Bulk	$0.38 \pm 0.03 \text{ J/cm}^2$	[8]
Silicon (100)	Bulk	$\approx 0.4 \text{ J/cm}^2$	[22]
Silicon (100)	Bulk	$0.41 \pm 0.04 \text{ J/cm}^2$	[23]
Fused Silica	Bulk	$4.58 \pm 0.54 \text{ J/cm}^2$	This work
Fused Silica	Bulk	$4.2 \pm 0.3 \text{ J/cm}^2$	[24]
Fused Silica	Bulk	$\approx 4.95 \text{ J/cm}^2$	[25]
Fused Silica [†]	Bulk	4.14 J/cm^2	[26]
Gold Film on Glass	25 nm	$0.80 \pm 0.25 \text{ J/cm}^2$	This work
Gold Film on Glass	30 nm	$1.11 \pm 0.09 \text{ J/cm}^2$	[27]
Gold Film on Glass	300 nm	$\sim 1.3 \text{ J/cm}^2$	[28]
Gold Film on Glass	500 nm	$1.08 \pm 0.15 \text{ J/cm}^2$	This work
Gold	Bulk	$0.92 \pm 0.10 \text{ J/cm}^2$	[23]
Gold	Bulk	$0.91 \pm 0.10 \text{ J/cm}^2$	[29]

[†]Molecular Dynamics – Calculated Threshold

To measure the reduction in the ablation threshold, we needed to know the gold ablation threshold without near-field enhancement effects. For this goal, we investigated the fs –laser ablation threshold for gold films of a variety of thicknesses. One would expect that the ablation threshold for a thin film would differ from the bulk material threshold due to physical interactions with underlying layers in the thin film case. For example, other studies have observed an increase in ablation threshold with film thickness up to an effective penetration depth [30]. Since the effective penetration depth is expected to be smaller than 100 nm for near-infrared light, the 500 nm thick film is expected to have similar ablation characteristics to a bulk sample, as we observed. Due to the similarities in values and overlapping uncertainties in the threshold measurements of the gold samples, we decided to use our threshold measurement for the 500 nm gold film as the ablation threshold of gold nanoparticles, while not neglecting the possibility that the size scale of the gold nanorod might have an effect on the ablation behavior.

2.4 Nanoscale surface mold

We developed a new method to measure the ablation depth profile for individual nanoablation sites by creating an inverse nanoscale mold of the ablation features on the silicon surface. We first thermally deposited an Au layer on the silicon surface at a rate of 0.5 nm/s to a final thickness of 25 nm. We then deposited a layer of chrome (Cr) on top of Au for adhesion without exposing the sample to air. By adhering a backing layer of glass to the Cr layer, we could peel the gold nanomold from the silicon surface. No release layer was necessary as the adhesion between Au and silicon is very weak. The inverse mold of the silicon surface topography thereby allowed us to measure ablation craters as raised protrusions rather than concave nanopits. Standard sharp AFM tips could then easily provide the profile of the raised protrusions, eliminating the need for fragile and costly ultrahigh resolution probes (e.g. carbon nanotube-tipped probes). Imaging raised protrusions also eliminated the difficulties associated with AFM imaging within nanoscale surface indentations. This new inverse nanoscale mold could serve as a reliable metrology technique for nanoscale studies. We validated the results

by comparing a set of known feature sizes in the original and molded surfaces, and observing that fidelity was preserved.

3. Computational simulations

We use the Discrete Dipole Approximation (DDA) method for all electrodynamic calculations in this study [31,32]. In DDA simulations, the simulated geometry is divided into small cubic regions, within which the induced dipole polarization is assumed to be uniform. The sum interaction of the dipole polarizations can be used to simulate the total interaction of light with the entire structure. DDA only simulates the structures of interest, and does not need to explicitly compute the boundary conditions and external regions. This difference in calculation technique makes DDA computationally efficient, but DDA is still an approximation. The approximation becomes exact as the dipole size becomes infinitely small. Researchers have implemented DDA successfully for many different applications in simulating light interactions with particles, including interstellar dust and colloidal nanoparticles [12,33,34].

We chose the DDA computation package ADDA, developed by Yurkin and Hoefstra at the University of Amsterdam, for our calculations because of demonstrated speed and efficiency, and access to parallel processing capabilities [35]. ADDA also allows easy access to dipole polarization vector data at each voxel, which is important for our calculations of electromagnetic fields at arbitrary locations. We wrote auxiliary Matlab programs to enhance the capabilities of ADDA for geometry generation and near-field calculation. Gold dielectric function values at the irradiation wavelength were obtained from a curve fit to experimentally determined dielectric constants [36]. We corrected these dielectric function values for size-related surface damping [37,38] according to the Drude equation with a modified damping constant. Our own calculations and those of others have shown that the FCD polarization prescription is superior for the calculation of interaction cross-sections for large refractive indices [39], but we have found that the LDR polarization prescription is able to render field calculations more accurately and with fewer artifacts, so we have used that DDA calculation method in all simulations. Since these findings are beyond the scope of this paper, we will be further addressing them in a different publication.

DDA calculates the interaction (absorption and scattering) cross-sections, which are a measure of the ability of a particle to remove light from the forward direction of propagation. The extinction cross-section, C_{ext} , is a sum of the scattering, C_{scat} , and absorption, C_{abs} , cross-sections (Eq. (1)). The interaction efficiency, Q_{ext} , is equal to the ratio of the electromagnetic interaction cross-section to the geometrical area, A , of the structure (Eq. (2)).

$$C_{ext} = C_{abs} + C_{scat} \quad (1)$$

$$Q_{ext} = \frac{C_{ext}}{A} \quad (2)$$

For plasmonic nanoparticles, the extinction efficiency can be much larger than one as the resonant interaction draws light towards the particle from a much wider area than the geometrical area. In all simulations, a unit intensity of light was incident in the negative z -direction on the simulated geometry.

We calculate the electric and magnetic near-field enhancements surrounding the nanoparticles from the superposition of the scattered and incident fields. The near-field enhancements are important for the understanding of near-field ablation because of their effect on decreasing the ablation threshold and controlling the ablation patterns and expected size scales. We compute the scattered fields resulting from the complex dipole polarizations using Green's tensor formulation for the interaction of point dipoles with Eqs. (3)–(4) [33,40].

$$\vec{E}_{scat,m} = \sum_{n \neq m}^N \frac{e^{ikR_{mn}}}{R_{mn}^3} \left\{ \left(3\hat{r}_{mn} (\hat{r}_{mn} \cdot \vec{P}_n) - \vec{P}_n \right) (1 - ikR_{mn}) + k^2 R_{mn}^2 \left((\hat{r}_{mn} \times \vec{P}_n) \times \hat{r}_{mn} \right) \right\} \quad (3)$$

$$\vec{H}_{scat,m} = \sum_{n \neq m}^N \frac{e^{ikR_{mn}}}{R_{mn}^3} (\hat{r}_{mn} \times \vec{P}_n) \{ k^2 R_{mn}^2 + ikR_{mn} \} \quad (4)$$

We use these equations to calculate the sum electromagnetic (E and H) field strength enhancement at point m for each dipole n , having a complex polarization P_n at a distance of R_{mn} in the direction from the dipole to the field point, r_{mn} , in incident light with a wave number k . We calculate near-field enhancements from dipole polarizations using a home-written program for Eqs. (3)–(4). The Poynting vector represents the direction of light propagation, and has the magnitude of the electromagnetic energy density at a given position. Our recent research has identified the Poynting vector magnitude as an accurate predictor for the PLN ablation threshold [8], thus we calculate this term in our current simulations from the electric and magnetic fields at each location.

3.1 Validation calculations

To estimate the accuracy of the DDA platform for the simulation of gold nanoparticles in the near-infrared, we first compared DDA results for spheres with the exact Mie calculations, which are available only for spheres [41]. For an isolated 50 nm gold nanosphere at the plasmon resonance condition ($\lambda = 532$ nm, in water), the errors in the absorption and scattering cross-sections were 8% and 5%, respectively, for a DDA simulation with 32 dipoles across the sphere diameter (17256 total dipole elements) as compared with the exact Mie solution. However, DDA tends to overestimate the absorption cross-section for large refractive indices. For example, for the same size sphere simulated at near-infrared wavelengths ($\lambda = 780$ nm) in an air environment with the same discretization, we observe larger relative errors (135%) compared with the exact Mie solution due to the larger absolute magnitude of the index of refraction present at longer wavelengths and increased relative index of refraction at the interface. The error for DDA calculations in the scattering cross-section remained relatively small for the same sphere (7%), indicating that DDA simulations are useful for scattering calculations even for large refractive indices.

The accuracy of DDA for the calculation of interaction cross-sections has been investigated in detail for general cases [32,42]. A recent and specifically relevant paper [39], studied the use of DDA for the simulation of gold nanoparticles in the near-infrared. Similar to our findings, they observed similar trends and found that the error in absorption cross-section could be large for gold nanoparticles at near-infrared wavelengths and that the filtered coupled dipole DDA solution method provided more accurate results for interaction cross-sections.

The accuracy for the cross-sections can be improved by decreasing the size of the cubic dipoles which make up the simulated nanoparticle, on account of two separate effects: better resolution of curvature as well as improving the fundamental accuracy of DDA. As the size of the dipoles decreases, corresponding to an increase in the number of dipoles across a given sphere diameter, the calculated cross-sections converge towards the exact value. When the number of dipoles across the sphere diameter is increased to 192 (3.7 million dipoles in total), the error in the scattering cross-section almost vanishes (1.2%), while the error in the absorption cross-section improves to 26%. Improved calculation accuracy does come at the cost of increased simulation time, however. In all cases, the predicted cross-section is larger than the Mie solution. DDA dipole cell sizes were kept at 1 nm or less in all cases to resolve particle curvature and to promote simulation accuracy. Early DDA studies proposed a figure of merit $|m/kd|$, where $|m|$ is the magnitude of the index of refraction, k is the wave vector and d is the side length of a single dipole cube. For this non-dimensional figure of merit, it was estimated that $|m/kd| < 1$ should yield accurate results [43]. In our nanorod simulations, the maximum $|m/kd|$ used was 0.026, implying good simulation solution accuracy. As described above, the error in the calculated absorption cross-section can be a concern for DDA calculations for gold nanoparticles at near-infrared wavelengths. However, our primary interest is in the calculated near-field intensity enhancements for which DDA has proved to provide accurate estimates as we will discuss next.

We subsequently compared the near-field enhancement patterns obtained by DDA to those predicted using Mie theory for a 50 nm gold sphere in air at 780 nm. The accuracy of near-fields calculated using DDA has not been well-studied, especially for magnetic fields and the Poynting vector. The results matched well both qualitatively and quantitatively. The error in fields ($|E|^2$, $|B|^2$, and $|S|$), calculated using DDA and compared with Mie theory, were confined primarily to the surface of the sphere. We compared the fields on a square grid of $150 \times 150 \text{ nm}^2$ (3 diameters square) in the central vertical cross-section, including both internal and external fields. The region calculated corresponds to plus and minus one diameter in the horizontal and vertical directions from the sphere surface, which is the region that near-fields enhancements are concentrated. We divided the difference in the calculated fields from DDA and Mie theory by the Mie theory values to obtain a relative error for each point. By adding up these values and dividing by the number of points, we obtain an average relative error for the region studied. Using this method, we found an average relative error of 16%, 1% and 6% for the $|E|^2$, $|B|^2$, and $|S|$ field magnitudes, respectively, for a sphere composed of 32 cubic dipoles across the diameter. These errors also decreased with decreases in the dipole cube size, to only 3%, 0.4% and 1.6% for the $|E|^2$, $|B|^2$, and $|S|$ field magnitudes, respectively for a sphere composed of 192 dipoles across the diameter. Using these simulations, we conclude that DDA can provide accurate field enhancement values for near-field calculations. Lastly, we expanded these validation studies to qualitatively compare DDA results with published studies on the interaction of light with particles on a surface. Specifically, we compared DDA particle-on-a-surface simulations to expanded Mie theory results from the literature [18,44,45]. Our studies showed morphological agreement with published enhancement patterns and scattering distributions for spheres on a surface.

3.2 Results – simulation of isolated rods

Figure 1 shows the simulated and experimental extinction spectra of the isolated nanorods. We directed significant effort towards obtaining accurate simulations of our gold nanorods, as was also determined necessary by Ungureanu *et al.* [46]. We investigated various sets of dielectric constants and nanorod dimensions and shapes, including flat-ended cylindrical, spherically-capped nanorods, and experimentally observed shapes. The red curve shown in Fig. 1 shows the simulated spectra using a spherically-capped cylinder, while the blue curve shows the more experimentally representative bone shape. The bone shape and size of the rods in the simulations were modeled to be representative of the experimentally observed shapes from a set of high-resolution SEM images, as described in the previous section. Specifically, we modeled the rods as ellipsoidally-capped ($e = 0.6$), cylindrically-symmetric shapes with an hourglass-like tapered midsection ($D_{\min} = 0.87 * D_{\max}$). We also simulated the random orientation of nanorods in a colloidal solution by averaging the extinction at four different orientations (along x, y, z axes and along $[1, 1, 1]$) for each of the simulated shapes.

Figure 1 shows that the simulations using the more realistic bone shape match experiment much better than the commonly used spherically-capped cylindrical shape. Using the Palik dielectric constants and representative bone shape, we found excellent agreement between the calculated peak position of the longitudinal resonance and the experimentally measured peak extinction. The overall spectrum shape also followed expected trends, with a peak at $\sim 510 \text{ nm}$ due to the transverse plasmon resonance. All subsequent simulations were done using the bone shape for the nanorods.

To take into account the effect of the observed size distribution of our nanorods in our calculations for the bone-shaped rods, we used a weighted average of the average nanorod ($28 \times 76 \text{ nm}^2$) with plus and minus two standard deviations in measured diameter and nanorod length. We found that modeling the size distribution resulted in the broadening and redshifting of the longitudinal plasmon resonance, in agreement with Prescott *et al.* [47]. The nanorod extinction peak redshifts when the size distribution is modeled because larger particles have larger absolute cross-sections, slightly skewing the peak towards longer wavelengths. The additional experimentally observed peak near 530 nm is due to cuboidal shapes and agglomerates observed in the colloid but not explicitly simulated.

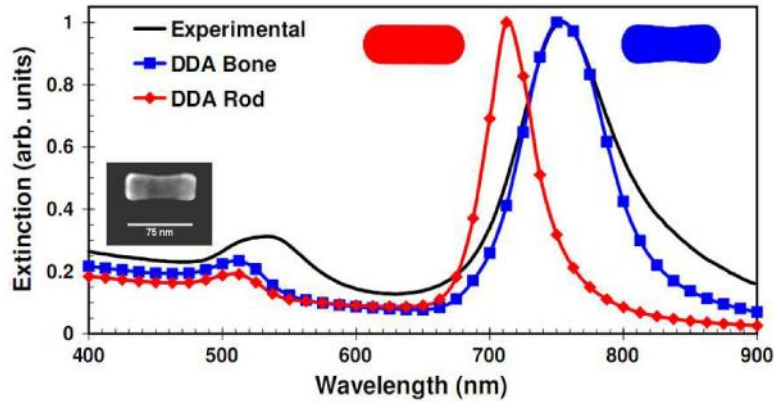


Fig. 1. Extinction Spectra of Gold Nanorods: The measured Vis-NIR extinction spectrum for gold nanorods as compared with simulated extinction spectra for two different rod shapes. The red curve represents a spherically-capped cylinder and the blue curve represents an ellipsoidally-capped bone. The inset shows a high-resolution SEM image of a single rod. It is clear that the bone shape reproduces both the extinction spectra and SEM appearance more accurately. Both sets of simulations were completed with the same length, maximum width, and overall aspect ratio as the measured average values of the nanorods (28×77 , $AR = 2.8$), but the bone-shaped rod simulation also includes the broadening effect of the observed nanorod size distribution ($28 \pm 4 \times 77 \pm 9$ nm, $AR = 2.8 \pm 0.3$), where the given ranges represent two standard deviations in nanorod size.

The exceptional agreement of the simulated results with experimental observations shows that DDA can be used to accurately simulate the plasmonic behavior of gold nanorods. It is important to note that only with the accurate modeling of the nanoparticle shape do the extinction spectra match. The extinction enhancement is accompanied by a large electromagnetic field enhancement in the near-field of the nanoparticle. As the nanorods are randomly distributed on the surface, it is important to understand the interaction efficiency and near-field enhancement of isolated rods as a function of the angle between the nanorod long axis and the polarization of the incident light. We therefore performed a numerical study of the enhancement and interaction efficiency compared with the polarization alignment angle for isolated particles and for particles on a surface. The results revealed a $\cos^2\theta$ dependence on interaction efficiency and peak enhancement with angle θ in both cases.

3.3 Results – simulation of nanorods on a surface

DDA simulations were expanded to simulate a nanorod on a silicon substrate in an air environment to study the near-field enhancement for plasmonic laser nanoablation. These simulations automatically take into account multiple reflections between a particle and surface, a critical aspect for particle on surface simulations [18]. The dimensions of the silicon substrate were $240 \times 190 \times 140$ nm³, centered beneath the particle (~ 10 million total dipoles). The computational simulations for nanorods on a silicon substrate included the presence of the 2 nm native oxide layer. We modeled the native oxide with the optical properties of silicon dioxide, as shown in Kim *et al.* [44], using tabulated data [36]. The cross-sectional area of the domain was large enough such that edge effects did not affect the near-fields around the particle. Adjusting the planar expanse or depth of the simulated substrate beyond this level changed the peak near-field enhancements by less than 10%.

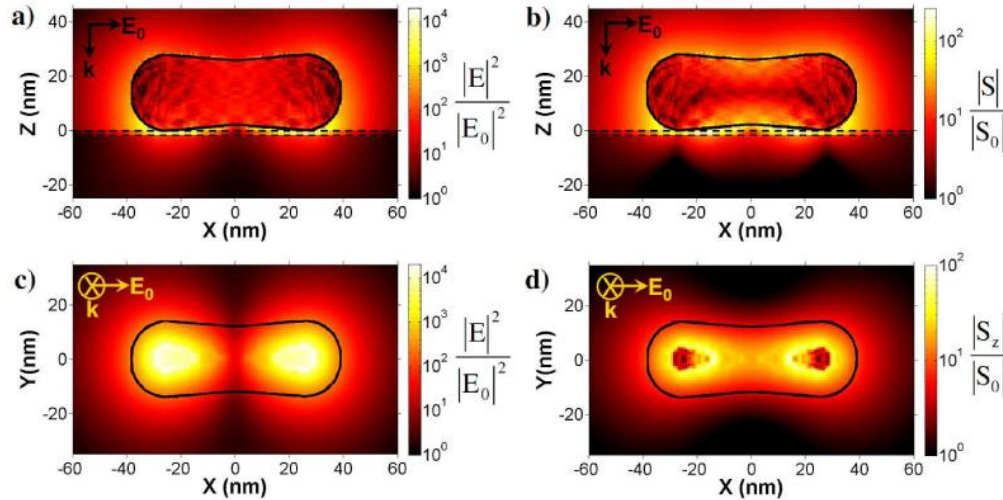


Fig. 2. Calculated near-field enhancement around a gold nanorod ($28 \times 77 \text{ nm}^2$) on a silicon substrate: Images a) and c) show the $|E|^2$ enhancement, while b) and d) show the enhancement in the Poynting vector magnitude $|S|$. The incident light has $\lambda = 780 \text{ nm}$ and its polarization is parallel to long axis of the nanorod. The images a) and b) show the enhancement in the central cross-section of the rod. Images c) and d) show the field enhancements in the top layer of the substrate. The black outline shows the initial position of the nanorod. Note that the substrate simulated is much larger than the expanse shown in a) – d).

Figure 2 shows the electromagnetic enhancement patterns around a nanorod on a silicon surface. The curved black solid lines show the outline of the particle, and the upper and lower dashed black dotted lines show the top of the substrate surface (2 nm thick layer of SiO_2) and the top of the silicon surface, respectively. In comparing the subplots a – d in Fig. 2, it is important to notice the differences between the $|E|^2$ and $|S|$ plots. The $|E|^2$ – field enhancements are two orders of magnitude larger than the $|S|$ for both the cross-sectional plots as well as for the enhancements on the top surface. The enhancement patterns are also clearly different. For the $|E|^2$ enhancement, there are two strong regions of enhancement near the end of the rod, while due to the effect of the magnetic field on the Poynting vector enhancement pattern, the $|S|$ enhancement is more distributed beneath the nanorod. The component of the Poynting vector normal to the surface has previously been identified as responsible for surface ablation [8,18]. We show the magnitude of the z – component of the Poynting vector, $|S_z|$, on the silicon surface in Fig. 2d, but show the total magnitude of the Poynting vector, $|S|$, in Fig. 2b because the normal component cannot be resolved in the perpendicular cross-section.

An additional study of the magnitude of $|E|^2$ and $|S|$ was performed as a function of angle between the nanorod long axis and polarization of the incident light. We again found a $\cos^2\theta$ dependence for the enhancement versus angle for nanorods on a surface. It should also be noted that the skin depth, or characteristic penetration length, of near-infrared light in gold at this wavelength is on the same length scale as the diameter of the nanorods in this study.

4. Experimental results

Gold nanorods were deposited on a silicon surface to study the effects of enhanced near-fields for surface ablation. Several sites on the silicon surface were targeted to observe a significant nanorod population. We irradiated the silicon at the center of each grid with a single laser pulse slightly above the silicon ablation threshold ($550 - 700 \text{ mJ/cm}^2$). We then calculated the fluence at the position of each uniquely identifiable nanorod using the distance from the center of the single shot ablation crater. By identifying the angle of each rod relative to the laser polarization, we determined the effective fluence along the long axis of the rods at each individual rod locations. Our goal was to study the effective fluence for nanorod survival,

nanorod removal, and plasmonic ablation of the silicon surface. Using this data, we found ablation thresholds and corresponding enhancements for PLN using gold nanorods on silicon.

4.1 Nanorod removal

Figure 3 presents the percentage of nanorod removal as a function of the effective fluence. We examined over 200 nanorod sites to check if each rod was removed or remained in place after laser exposure. Each result was placed into logarithmically spaced fluence bins, containing at least 10 nanorods. Each data point in Fig. 3 represents the percentage of rods removed in the fluence bin, and the fluence is given as the average of the rods within that bin. Unlike for spheres, the energy coupling of laser light with the rods is polarization-dependent. As discussed above, the near-field enhancement and absorption and scattering cross-sections scale as $\cos^2\theta$ multiplied by the maximum values for an aligned nanorod. By applying a $\cos^2\theta$ multiplier on the fluence, we estimated the effective fluence that each rod actually contributed to the longitudinal resonance. This correction collapsed the randomly scattered data into a single trend. The errors shown for each data point correspond to the size of each bin for the x axis and the standard deviation of the number of nanorods in each fluence bin for the y axis.

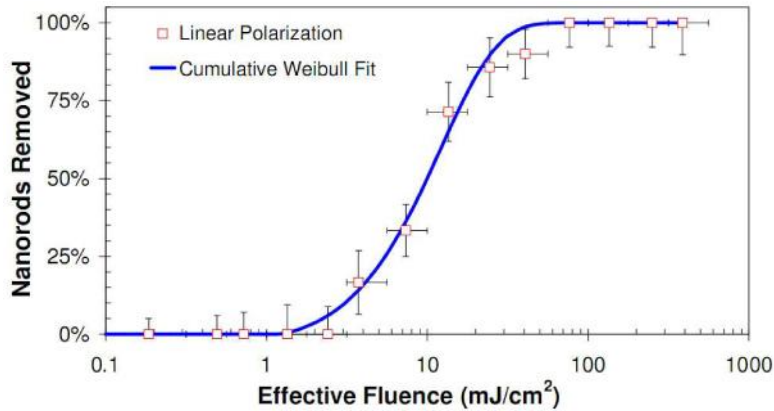


Fig. 3. Nanorod removal from a silicon surface: The percentage of nanorods removed following single-shot irradiation as a function of the effective local fluence (peak fluence) for linearly polarized laser light with cumulative Weibull fits. The data points present nanorod outcomes grouped into logarithmic fluence bins. We calculated the effective peak fluence by multiplying the local fluence by the $\cos^2\theta$ of the angle between the polarization and nanorod long axis.

Due to statistical variations in rod size, aspect ratio, and shape, the thresholds for rod removal and ablation are statistical estimates. To model the statistical trend of our results, we fit the nanoparticle removal data using a Weibull cumulative damage equation [48]. The Weibull damage equation, more commonly used in materials failure analysis, fits the failure probability of inhomogeneous samples to a given load according to Eq. (5).

$$P_R = 1 - e^{-\left(\frac{F - F_{th}}{F_0}\right)^\beta} \quad (5)$$

Here, the nanoparticle removal probability, P_R , gives the percentage of rods removed for a given fluence value. The exponent, β , is a measure of the sample homogeneity and increasing β results in a narrower transition width. In our application of this equation, the applied stress is given by the laser fluence, F . The parameters for fitting include a nanorod removal threshold of $F_{th} = 1.2 \text{ mJ/cm}^2$, a characteristic removal value of $F_0 = 12.2 \text{ mJ/cm}^2$, when $1/e$ rods (63%) have been removed, and a β value of 1.2. The width of the transition from no removal to the removal of all nanorods can be explained by the differences in enhancement for various size nanorods. The same experiment was also performed using circularly polarized light. In this experiment, we did not observe any angular dependence with the orientation of

nanorods (as expected), and found that the plasmon resonance coupling was much less efficient as a result of the continuously shifting polarization direction. For circularly polarized light, the Weibull coefficients were $F_{th} = 8.9 \text{ mJ/cm}^2$ and $F_0 = 210 \text{ mJ/cm}^2$ with a β value of 1.6. The β value is increased for the circularly polarized case because a degree of freedom has been removed, leading to an effectively more homogenous sample.

We attribute the nanorod removal to the ablation of the gold rod itself as a result of the enhanced intensities in its surface. To find the observed enhancement with these experiments, we compare the characteristic removal value ($F_0 = 0.012 \text{ J/cm}^2$) for the gold nanorods with the ablation threshold observed for the 500 nm thick gold thin film ($1.08 \pm 0.15 \text{ J/cm}^2$). Assuming that the characteristic removal value is representative of an average rod on the surface, we obtain an enhancement of $\sim 89 \pm 13$. The ablation threshold for gold nanoparticles may be lower than the threshold for bulk gold considering of size confinement and electrical isolation. Nevertheless, the enhancement value agrees within the margin of error with the peak enhancement in the Poynting vector magnitude within the nanoparticle on a silicon surface, which has a peak value of ~ 100 . In addition to this agreement, the removal of many nanorods outside the direct silicon modification region implies that near-field effects were responsible for their complete removal.

Other possible mechanisms for the nanoparticle removal include heating-related effects such as nanoparticle melting and its complete evaporation, explosive boiling, or surface heating/expansion resulting in nanoparticle ejection. In the case of nanoparticle ejection, however, we would expect to observe displaced nanoparticles somewhere on the silicon substrate, none of which were ever observed in our experiments. Assuming no heat transfer out of the particle during the laser pulse and using the absorption cross-section for an isolated nanorod of $28 \times 76 \text{ nm}^2$ simulated with 192 dipoles across the nanorod diameter, the threshold for the complete particle melting would be $\sim 37 \text{ mJ/cm}^2$, which is more than three times greater than the experimental characteristic removal threshold. We hypothesize that the time scale for PLN is much shorter than for a heat transfer-mediated nanorod removal. Plasma formation can occur within $\sim 1 \text{ ps}$ for ultrafast pulses [49], while melting does not occur until the electrons transfer absorbed energy to phonons, which occurs $\sim 30 \text{ ps}$ after the laser pulse for a gold nanorod [50]. If the rods are ablated by PLN, they will be removed through plasma expansion. We also note that if the heating was responsible for nanoparticle removal, there should be a fluence zone where nanorods become spherical due to melting. We therefore reason that nanoparticle ablation will occur prior to and at lower fluences to melting, boiling, or surface expansion and ejection, even if the threshold is reached for nanoparticles on a surface. We thus conclude that complete ablation of the nanorods is the cause of removal.

4.2 Silicon surface ablation

We observed nanoscale laser modification and ablation of the silicon surface at local fluences significantly lower than the direct fs-laser ablation region of silicon ($10 \text{ mJ/cm}^2 < F < 420 \text{ mJ/cm}^2$). The efficiency of the ablation in this regime depended on the orientation of the rod relative to the incident laser polarization. We studied the nanoablation sites using high-resolution SEM to determine the nanocrater lateral dimensions and AFM to measure the nanocrater depth profiles.

Figure 4 show SEM images of nanoscale ablation site and a depth profile as observed by an AFM. Within the direct fs-laser modification region of silicon (at $F > 420 \text{ mJ/cm}^2$), the nanorod ablation sites were local semispherical craters. Outside the silicon ablation threshold, we found that the nanorod ablation sites were photo-imprints of the nanorod, very similar in size to the nanorod, as shown in Fig. 4a. This is an interesting result, because the ablation sites did not consist of two separate craters for any of the plasmonic ablation sites, even for sites very close to the ablation threshold. We interpreted this result as evidence that the Poynting vector magnitude dominated the ablation morphology. We created nanoablation feature widths as small as 22 nm (Fig. 4a), representing the creation of $\lambda/35$ features using plasmonic near-field enhancement. Near the plasmonically-enhanced threshold, the ablation is confined

to a very small and shallow region beneath the nanoparticle, as expected from DDA simulations.

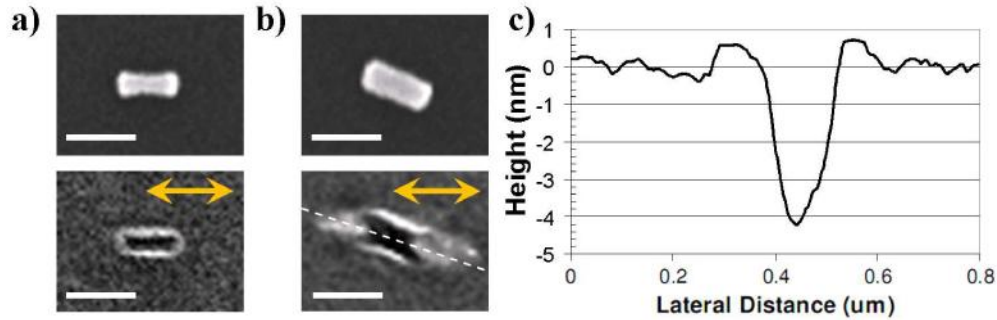


Fig. 4. Nanoscale ablation site and depth profile: SEM images of the nanorods before and after laser irradiation at a local effective fluence of a) 54 mJ/cm^2 , right at the ablation threshold, and b) 218 mJ/cm^2 . The scale bars correspond to 75 nm and the yellow arrows indicate the incident polarization. c) The depth profile of the ablation site shown in (b), along the long axis shown with the dotted line as obtained using AFM. Note the different scales for the horizontal and vertical axes in (c).

As can be seen in Fig. 4, a small rim was present at the edges of the nanoablation sites. This rim, previously described for the direct laser ablation of dielectrics [51], is caused by the melting of a thin surface layer beneath the surface volume at a fluence below the ablation threshold, which then is pushed to the edges of the ablation crater due to the high-pressure expanding plasma within the crater. We examined several nanoablation sites with ultrahigh resolution SEM and energy dispersive X-ray spectroscopy (EDS) for traces of gold in the crater. The results showed no gold at the crater rim or ablation sites within the limits of the system sensitivity, implying that the nanoparticle was completely removed from the ablation site.

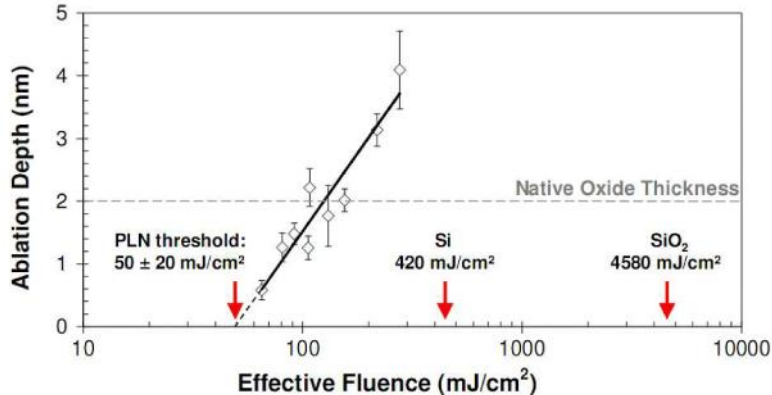


Fig. 5. PLN threshold of silicon: Logarithmic dependence of ablation depth as a function of peak fluence at various sites where nanorods were present before the irradiation. Extrapolation of the linear fit to zero provides the single-shot ablation threshold ($50 \pm 20 \text{ mJ/cm}^2$) for nanorod-enhanced PLN. The direct fs-laser ablation thresholds of silicon and silica are also given for comparison with the PLN threshold. The dashed gray line describes the thickness of the native oxide layer on silicon.

To estimate the threshold for PLN of silicon by a gold nanorod, we plot the depths (h_a) of nanorod ablation sites as a function of the effective local fluence, shown in Fig. 5, for a region outside of the direct fs-laser ablation of silicon. The effective fluence represents the portion of the incoming laser field aligned with the long axis of the gold nanorods. The results show a

linear relationship between the depth of the nanoablation sites and the logarithm of the effective fluence, shown in Eq. (6) [8].

$$h_a = \alpha_{eff}^{-1} \ln \left(\frac{F}{F_{th}} \right) \quad (6)$$

Using this data and the Eq. (6), we find an effective optical penetration depth, α_{eff}^{-1} , of 2.2 nm, as compared to a $\alpha_{eff}^{-1} = 129$ nm for ultrafast laser ablation of silicon without plasmonic enhancement, which was found from our direct fs-laser experiments on silicon (Table 1). This difference shows the localization of plasmonically-enhanced fields around the nanoparticle and that the ablation is mainly confined to the thin oxide layer. The linear fit gives an ablation threshold, F_{th} , estimate of 50 ± 20 mJ/cm², where the error is calculated from linear regression analysis. This reduction in the ablation threshold reveals a plasmonic enhancement of ~8 times when compared to the direct fs-laser ablation of silicon. This experimental enhancement is much lower than expected from our simulation results. A significant proportion of the ablation, however, occurs within the top native oxide layer, shown with the dashed gray line in Fig. 5, for the sites studied here. If we model the native oxide as pure SiO₂, the calculated enhancement is much more substantial for the surface ablation, which is found to be ~92 using our experimental direct fs-laser ablation threshold for fused silica. This magnitude of enhancement matches the Poynting vector enhancement of ~100 (Fig. 2d) much better than the $|E|^2$ enhancement of ~10,000 (Fig. 2c).

In addition, we observe the better match of the ablation shape with the distribution of the Poynting vector, and we thus conclude that the Poynting vector magnitude is a better predictor of ablation behavior for PLN. This conclusion is in opposed to previous work that has taken the $|E|^2$ – field as the identifier for ablation [7,19], but is in agreement with our previous study using gold nanospheres on a silicon surface [8]. In that work, we also showed that the ablation enhancement matched the magnitude of the Poynting vector on the surface. By using asymmetric gold nanorods here, we can conclusively show that the ablation pattern and enhancement match the Poynting vector magnitude better than the $|E|^2$ – field enhancement.

5. Conclusions

In this paper, we have investigated the origin of the near-field enhancement for plasmonic laser nanoablation (PLN) using gold nanorods on a silicon surface. By using realistic shapes for our nanoparticle model, we were able to effectively simulate plasmonic nanoparticle enhancement behavior. From a comparison of experimentally observed nanorod nanoablation sites with simulations, we determined several parameters of importance. First, PLN with nanorods is orientation dependent and interaction scales as $\cos^2\theta$, where θ is the angle between the nanorod long axis and the direction of polarization for nanorods on a surface. Second, we observed nanorod removal due to ablation following a statistical trend based on the nanorod size distribution and associated variation in the plasmonic enhancement. PLN with nanorods was demonstrated capable of creating nanoscale features as small as 22 nm in width on a silicon surface. The minimum feature size was found to be a photo-imprint of the nanorod, and no physical limitations should prevent the creation of even smaller features using smaller nanorods. Third, PLN with nanorods can be achieved with a laser fluence threshold of ~8 times less than the silicon ablation threshold, and ~92 times less than the silicon dioxide threshold. Finally, we conclude that the Poynting vector enhancement more accurately predicts plasmonic laser ablation than the $|E|^2$ enhancement pattern, both in terms of ablation morphology and the magnitude of enhancement. This research can be useful for predicting damage to structures and biological materials in the vicinity of nanoparticles.

Acknowledgements

The authors would like to acknowledge the creators of the publicly available ADDA code for the useful software and thank Maxim Yurkin specifically for his helpful correspondence. Thanks to Nick Durr for the spectroscopic measurements and Neil Everett for assistance with

the nanomold fabrication. This work is supported by NSF Career Award CBET-0846868. We used equipment at the Center for Nano and Molecular Science at the University of Texas at Austin throughout this study.